Research Article Vol. 33, No. 25 / 15 Dec 2025 / Optics Express 53618
Optics EXPRESS

Stacked nanogap plasmons for multispectral photoluminescence

CHENG CHEN,[1] HWANHEE KIM,[1] DARYLL J. C DALAYOAN,[1] SUNGHWAN KIM,[1] SEONHYE EOM,[1] SEON NAMGUNG,[1] HYEONG-RYEOL PARK,[1,3] AND DUKHYUNG LEE[2,4]

[1]*Department of Physics, Ulsan National Institute of Science and Technology, Ulsan 44919, Republic of Korea*
[2]*School of Applied and Engineering Physics, Mohammed VI Polytechnic University, Ben Guerir 43150, Morocco*
[3]*nano@unist.ac.kr*
[4]*dukhyung.lee@um6p.ma*

Abstract: Plasmonic metasurfaces supporting multiple resonances are highly desirable for enhancing optical fields at distinct wavelengths. Here, we demonstrate doubly stacked nanogap arrays that exhibit dual Fabry–Pérot resonances of the gap plasmons. Numerical simulations reveal that both resonances appear at different wavelengths due to the lateral length difference between the upper and lower nanogaps. Furthermore, we fabricated stacked nanogap arrays by alternating metal-insulator deposition, electron beam (e-beam) lithography, and ion milling. Due to the dual plasmon resonance, the photoluminescence spectra of spin-coated dyes (R6G and IR-820) show distinct modifications near the two reflection dips. These results highlight stacked nanogaps as a promising platform for co-localized multicolor dye excitation and multispectral photoluminescence engineering, with potential applications in multi-wavelength light sources and multicolor displays.

1. Introduction

Plasmonic metasurfaces have been extensively studied for their ability to concentrate light into sub-wavelength volumes, enabling applications such as photoluminescence (PL) modification [1,2], surface enhanced Raman spectroscopy (SERS) [3–6], and diverse nonlinear optical phenomena [7–10]. To extend these capabilities across multiple wavelengths, metasurfaces with multiple resonances have been widely explored [11–14]. For example, broadband PL from silicon was achieved by exploiting higher order modes of the plasmonic cavity [15]. Gap plasmons in metal-insulator-metal (MIM) waveguides are particularly attractive, as they provide strong field confinement and enhancement by squeezing light into nanometer-scale volumes [16–19]. Since the Fabry–Pérot resonance of gap plasmons is determined by the length and width of the waveguide [20–22], metasurfaces with multiple resonances can be realized by integrating MIM structures of different dimensions. Previous studies have demonstrated vertically stacked MIM nanogaps composed of alternating metal and dielectric layers, where different gap widths were engineered to produce multiple resonances, achieving strong SERS enhancement [23–25]. In addition to these multi-resonant designs, plasmonic gaps on flexible substrates with mechanically controllable gap widths have recently been demonstrated, enabling dynamic resonance tuning and selective enhancement of specific Raman modes [26].

In this work, we present vertically stacked metal-insulator-metal-insulator-metal (MIMIM) arrays with gradually decreasing lateral lengths, where the resulting difference between upper and lower nanogaps enhances dual Fabry–Pérot resonances. We investigated their optical properties using finite element method simulations with varying geometrical factors, showing how to tune the resonances. We also demonstrated the fabrication of trapezoidal MIMIM stack arrays by

#580493 https://doi.org/10.1364/OE.580493
Journal © 2025 Received 29 Sep 2025; revised 1 Dec 2025; accepted 6 Dec 2025; published 12 Dec 2025

Optics EXPRESS

exploiting the inherent characteristic of ion milling, which preferentially removes material from the upper layers. The fabricated samples exhibited two distinct dips in the reflection spectra, corresponding to the Fabry–Pérot resonances predicted by the simulations. PL modification due to the field enhancement was further confirmed using two dyes, Rhodamine 6G (R6G) and IR-820, whose emission spectra overlap with the respective gap plasmon resonances. Our vertically stacked MIMIM architecture enables multispectral PL control through two co-localized Fabry–Pérot gap-plasmon resonances, offering a compact alternative to single-color multilayered metasurfaces [27] by achieving dual-wavelength functionality within a single structure.

2. Simulation results

Stacked nanogaps we studied are schematically described in Fig. 1(a). We have chosen gold and alumina (Al_2O_3) as metal and insulator materials because of their broad usage in plasmonics [28–30]. Especially, thickness of alumina layers can be controlled in an angstrom scale by using atomic layer deposition (ALD). The nanogap arrays can be specified by following geometrical parameters: gap width g of upper and lower nanogaps, bottom gold length l, inter-stack distance d, sidewall slope θ, and stack height h. To simplify the analysis, we fixed the height h at 110 nm in all simulations presented in this work. Simulated reflection, absorption, and field enhancement spectra for a representative case are shown in Fig. 1(b). Three distinct reflection dips and corresponding absorption peaks are observed at around 0.55, 0.7 and 0.9 µm. While the feature at 0.55 µm is attributed to the interband transitions of gold [31], the latter two features arise from the Fabry–Pérot resonances of gap plasmons confined within the upper and lower nanogaps [32–35]. Investigation of the field enhancement at each gap entrance clearly shows that Fabry–Pérot resonances occur independently in the upper and lower gaps due to their length difference. At a wavelength of 0.7 µm, only the upper gap exhibits significant field enhancement, whereas at 0.9 µm, only the lower gap does. Figure 1(c) shows the field map of the unit cell at the wavelengths corresponding to the respective maximum field enhancements. Characteristic

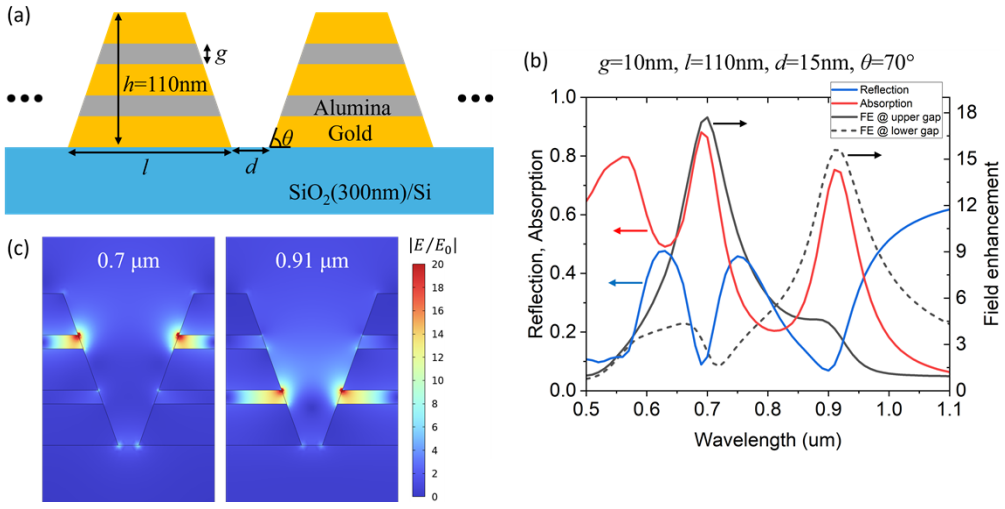

Fig. 1. Concept of stacked nanogap arrays studied in this work. (a) Schematic of the trapezoidal MIMIM arrays. (b) Simulation results for the optical properties with representative geometrical parameters (10 nm gap width g, 110 nm bottom gold length l, 15 nm inter-stack distance d, 70° sidewall slope θ). Field enhancement values were obtained by averaging at the respective gap entrances (alumina-air interfaces). (c) Field distributions at the wavelengths of maximum field enhancement for the upper and lower nanogaps.

Optics EXPRESS

field distributions of fundamental Fabry–Pérot resonances are observed in both field maps, with antinodes at the gap ends and a node at the center.

The field enhancements can be exploited to modify the PL of molecules located in the vicinity of the gap entrances, if the gap plasmon resonances are properly overlapped with the intrinsic PL spectrum [36–39]. Therefore, we studied the tunability of the resonances for various geometrical parameters. The simulated results are summarized in Fig. 2, where the geometrical parameters are identical to those in Fig. 1(b), except for the varying parameter. Figure 2(a) shows that the resonances redshift as the gap width g decreases, since a narrower gap yields a larger propagation constant for a given frequency. Furthermore, narrower gaps tend to produce higher field enhancements. Increasing the bottom gold length l (Fig. 2(b)) also induces redshifts, although this has little effect on the magnitudes of the field enhancements. Increasing the sidewall slope θ increases the lengths of both gaps, with a greater rate of increase for the upper gap. This becomes evident when comparing Fig. 2(b) and 2(c). From the simulations varying l and θ, a linear relation between the nanogap length and the resonance wavelength can be established, providing predictability of the Fabry–Pérot resonance wavelength for a given nanogap length (see Supplement 1 S1). Figure 2(d) shows that the resonances are largely unaffected by changes in the inter-stack distance d, confirming that the gap width and length are the primary determining factors for the Fabry–Pérot resonances.

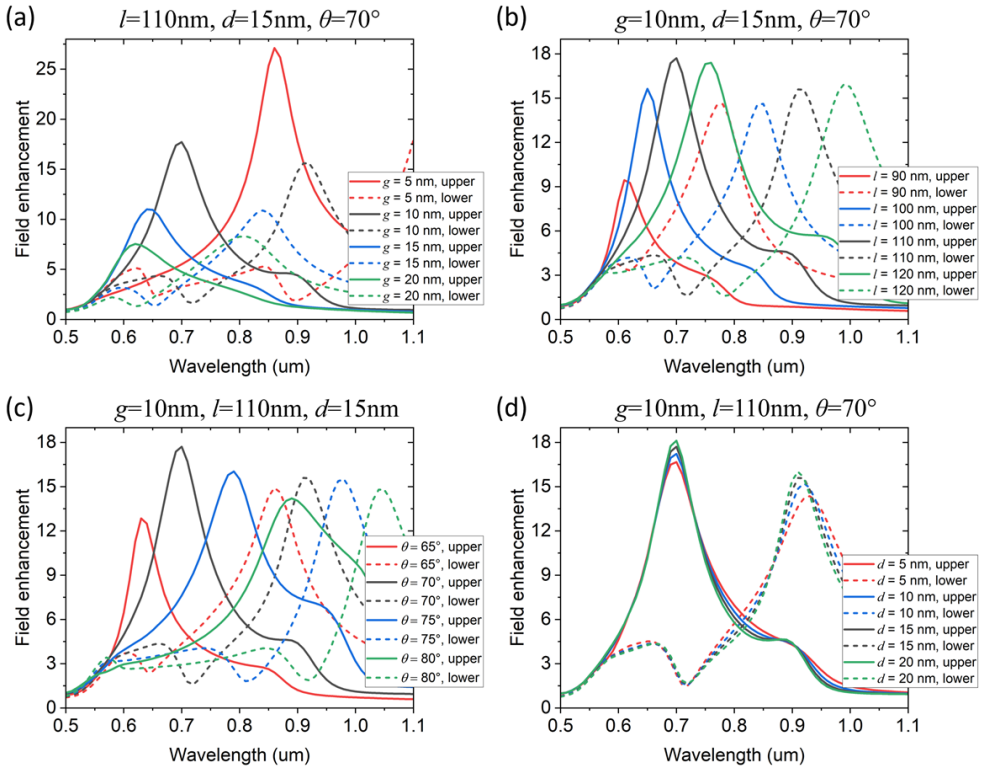

Fig. 2. Tunability of the gap field enhancements. Dependence on the (a) gap width g, (b) bottom gold length l, (c) sidewall slope θ, and (d) inter-stack distance d. Default values for the geometrical parameters are $g = 10$ nm, $l = 110$ nm, $d = 15$ nm, $\theta = 70°$. The solid and dashed lines denote the upper and lower gaps, respectively.

Optics EXPRESS

3. Fabrication and photoluminescence measurement

To realize the optical functionality shown in the simulation results, we fabricated MIMIM stacked nanogap arrays with structural parameters close to those in the simulations. Figure 3(a) illustrates the three-step top-down fabrication method [40]. First, 30 nm-thick gold layers and 10 nm-thick alumina layers were alternately deposited on an oxidized Si substrate by electron-beam evaporation and ALD at 200 °C using trimethylaluminum (TMA) and H_2O as precursors, respectively, forming the MIMIM film. The Al_2O_3 growth rate was approximately 1.4 Å per cycle (≈70 cycles for 10 nm). The optical dielectric constants (ε_r) of the deposited Al_2O_3, determined from ellipsometry measurements, were approximately 3.03 and 3.01 at 532 nm and 633 nm, respectively, corresponding to refractive indices of n ≈ 1.742 and n ≈ 1.736. Second, a PMMA mask with lines approximately 10 nm wide was patterned using electron-beam lithography (EBL) for the subsequent milling step. PMMA was spin-coated on the MIMIM film and baked at 180 °C for 1 min, followed by e-beam writing and development. Third, argon ion milling was carried out to etch the lines defined by the PMMA mask, yielding a trapezoidal MIMIM stack array. After the milling process, the PMMA mask was removed by acetone rinsing and O_2 plasma treatment. To examine the fabricated nanogap arrays, scanning electron microscopy (SEM) images were acquired. As shown in Fig. 3(b-d), the top-view images verify the formation of the stacked nanogap array across an area of 20 µm × 20 µm. The cross-sectional view in Fig. 3(e) reveals a period of 130 nm and an inter-stack distance of ~10 nm. The trapezoidal geometry is clearly observed, with the upper nanogaps having shorter lateral lengths than the lower ones.

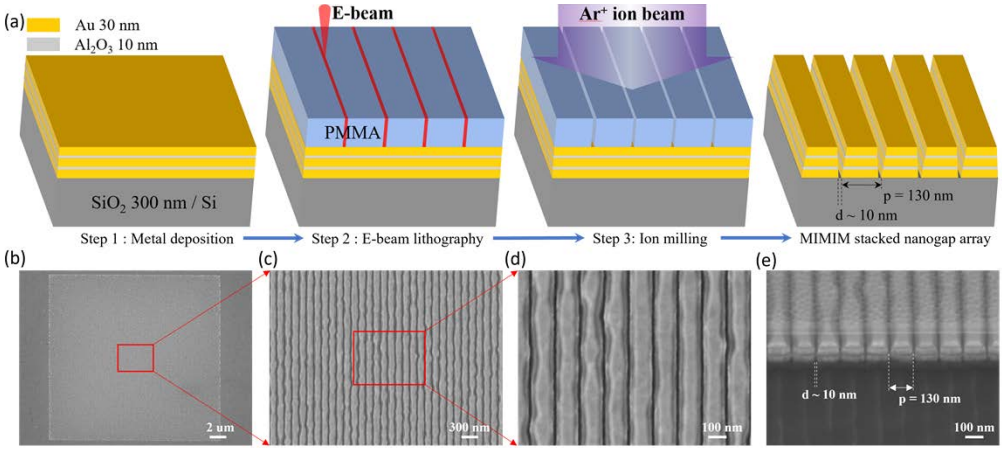

Fig. 3. Fabrication of MIMIM stacked nanogaps. (a) Schematic flow of the fabrication process. Au/Al_2O_3/Au/Al_2O_3/Au layers were deposited on a Si substrate with a 300 nm SiO_2 top layer, followed by e-beam lithography and argon ion etching to separate stacks. (b,c,d) Top view SEM images showing a 20 µm by 20 µm stacked nanogap array (e) Cross-sectional SEM image of MIMIM stacks. The period and inter-stack distance were estimated to be 130 nm and 10 nm, respectively.

To demonstrate that each of the dual plasmon resonances can modify PL spectra, two sets of samples were prepared for R6G [41,42] and IR-820 [43] dye molecules, respectively. Within each sample set, the e-beam exposure dose was adjusted to produce varying lateral dimensions. Due to the proximity effect [44,45] in EBL process, increasing the dose resulted in a wider exposed linewidth in the PMMA mask, leading to an increase in the inter-stack distance *d* and a decrease in the lateral size of staked nanogaps. Decreases of lateral sizes with increasing dose were confirmed by SEM images, as shown in Figs. 4(c,f) (see Supplement 1 S2 for the curve of inter-stack distance *d* versus EBL dose). We first measured reflection spectra to identify the

Optics EXPRESS

positions of plasmon resonances and proceeded PL measurements with spin-coated dyes. The reflection spectra of the first sample set for R6G are shown in Fig. 4(a). The reflection dips observed below 500 nm originate from the intrinsic properties of gold and are not associated with gap plasmon excitation, as discussed in the simulation section. For the sample with a 120 pC/cm dose, we can identify reflection dips at the wavelengths of ~645 nm and ~960 nm, which can be attributed to gap plasmon excitation at the upper and lower nanogaps, respectively. As indicated by the dashed line for the upper gap resonance, larger lateral dimensions with lower doses exhibited redshift of the resonance dips, which is consistent with the simulation results given in Fig. 2(b). For PL measurements, the first set samples were spin-coated at 2000rpm for 1 min with an R6G solution (10^{-4} M in ethanol), followed by solvent removal through heating on a hot plate at 60 °C for 5 min, leaving only the R6G molecules. PL measurements were conducted using a home-built setup with a 532 nm unpolarized excitation laser at a power of 1 mW and 1 μm laser spot size. The measured PL spectra are presented in Fig. 4(b). For reference, the PL spectrum of R6G on a plain gold film was also measured (black curve), showing that the intrinsic emission range is well overlapped with the resonance range of the upper nanogaps. In comparison to the intrinsic PL spectrum, the PL spectra from the stacked nanogap samples display modified spectral profiles, accompanied by intensity enhancements. The PL enhancement factor (EF)

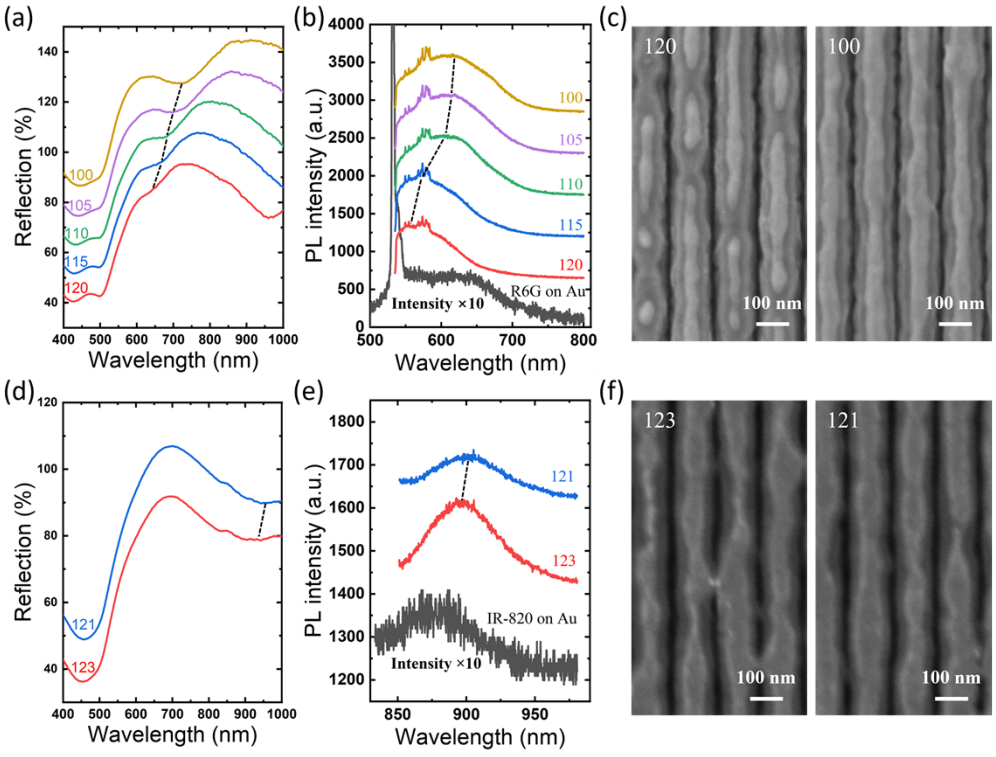

Fig. 4. Resonance tuning and corresponding PL modulation. (a) Reflection spectra measured from a set of stacked nanogap arrays fabricated using varying line doses (100–120 pC/cm) in e-beam lithography. (b) PL spectra of the sample set in (a) after spin-coating of R6G dye. The black curve represents the PL spectrum from an unpatterned gold film coated with R6G, scaled by a factor of 10 for clarity. (c) SEM top view images of stacked nanogap arrays, corresponding to line doses of 120 and 100 pC/cm. (d-f) Reflection spectra, PL spectra, and SEM images from another sample set fabricated with varying line doses (121–123 pC/cm) and spin-coated with IR-820 dye. Spectra in (a,b,d,e) have been vertically offset for clarity.

Optics EXPRESS

was calculated as EF = I_{MIMIM} / I_{Au}, where I_{MIMIM} and I_{Au} denote the integrated PL intensities from the MIMIM stacked nanogap arrays and the unpatterned Au film, respectively. For the first sample set fabricated with line doses ranging from 120 to 100 pC/cm, the corresponding EF values were 12.2, 13.6, 13.8, 13.6, and 13.1. These EF values were determined from the total PL emission, which includes contributions from both nanogap and non-nanogap regions, thereby providing a realistic measure of the overall enhancement. Notably, the PL measurements showed excellent spatial homogeneity across the MIMIM stacked nanogap array (Supplement 1 S3). Furthermore, the PL spectra exhibited a progressive redshift with increasing lateral length, analogous to the behavior of the reflection dip. This strongly indicates that the PL of R6G was modified through gap plasmon excitation at the upper nanogap.

For PL measurements of IR-820 dye, samples were fabricated with two different exposure doses, 123 pC/cm and 121 pC/cm. The reflection spectra shown in Fig. 4(d) reveal excitation of the lower nanogaps around 900-950 nm, again demonstrating the redshift associated with decreasing exposure dose, as indicated by the dashed line. In this second sample set, the upper nanogap resonance was diminished, possibly due to the fabrication imperfections such as fluctuations in the sidewall slope θ (see Supplement 1 S4) and proximity of the resonance to the region of interband transitions. Spin-coating of IR-820 was performed using a 10^{-3} M solution in ethanol, under the same spin-coating and solvent removal conditions as those used for R6G. PL measurements for IR-820 dyes were performed using a 633 nm unpolarized excitation laser at a power of 0.224 mW, and the results are presented in Fig. 4(e). The intrinsic PL spectrum obtained with a plain gold film (black curve) shows a good spectral overlap with the lower nanogap resonances. As in the case of R6G, the PL spectra from the stacked nanogap arrays exhibited enhancement, with EF values of 14.2 and 7.2 for line doses of 123 pC/cm and 121 pC/cm, respectively. Furthermore, the PL spectra showed a redshift of the peak position with decreasing exposure dose. This behavior, consistent with that observed in the reflection spectra, confirms that the PL of IR-820 was modified by the plasmonic resonance of the lower nanogap.

4. Conclusion

We have demonstrated that vertically stacked MIMIM nanogap arrays with tapering width along the height can support dual Fabry–Pérot gap plasmon resonances originating from the upper and lower nanogaps. By systematically varying the electron-beam exposure dose during lithography, we controlled the lateral dimensions and tuned the resonance wavelengths, resulting in predictable spectral shifts consistent with finite-element simulations. PL measurements using R6G and IR-820 dyes confirmed co-localized excitation and enhancement at two distinct resonances, verifying that the upper and lower nanogap plasmons can selectively influence the PL response of each dye. These results highlight the capability of stacked nanogap metasurfaces for simultaneous dual-wavelength control and multispectral light–matter interaction engineering. Furthermore, while EBL was employed here for nanoscale patterning, the design is fully compatible with nanoimprint lithography, providing a scalable and cost-effective route toward multi-wavelength light sources, color-selective photonic elements, and advanced multicolor displays.

Funding. National Research Foundation of Korea (2022M3H4A1A04096465, RS-2023-00257666, RS-2024-00353252, RS-2024-00454894, RS-2025-02272971); Korea Planning & Evaluation Institute of Industrial Technology (KEIT, RS-2025-06642983); Institute for Information Communication Technology Planning and Evaluation (IITP) (RS-2023-00259676, RS-2025-25464481); Ulsan National Institute of Science and Technology (1.250007.01).

Acknowledgments. We thank the UNIST Office of Research Facilities and Training (ResFacT) for their support in using the equipment.

Disclosures. The authors declare no conflicts of interest.

Data availability. Data used in this study are available from the corresponding author upon reasonable request.

Supplemental document. See Supplement 1 for supporting content.

Optics EXPRESS

References

1. Y. Koo, D. K. Oh, J. Mun, *et al.*, "High momentum two-dimensional propagation of emitted photoluminescence coupled with surface lattice resonance," Light:Sci. Appl. **14**(1), 218 (2025).
2. Z. Wang, Z. Dong, Y. Gu, *et al.*, "Giant photoluminescence enhancement in tungsten-diselenide-gold plasmonic hybrid structures," Nat. Commun. **7**(1), 11283 (2016).
3. J. Yun, H. Yu, and W. Nam, "Plasmonic Nanolamination for High-Performance SERS Substrates Based on Vertically Stacked 3D Multiple Nanogaps," ACS Appl. Nano Mater. **8**(10), 5028–5036 (2025).
4. W. Nam, J. Song, S. A. Safiabadi Tali, *et al.*, "Au/SiO2-Nanolaminated Plasmonic Nanoantennas as Refractive-Index-Insensitive and Transparent Surface-Enhanced Raman Spectroscopy Substrates," ACS Appl. Nano Mater. **4**(3), 3175–3184 (2021).
5. L. P. Hackett, W. Li, A. Ameen, *et al.*, "Plasmonic Metal–Insulator–Metal Capped Polymer Nanopillars for SERS Analysis of Protein–Protein Interactions," J. Phys. Chem. C **122**(11), 6255–6266 (2018).
6. Y. Q. Cao, K. Qin, L. Zhu, *et al.*, "Atomic-Layer-Deposition Assisted Formation of Wafer-Scale Double-Layer Metal Nanoparticles with Tunable Nanogap for Surface-Enhanced Raman Scattering," Sci. Rep. **7**(1), 5161 (2017).
7. N. Maccaferri, A. Zilli, T. Isoniemi, *et al.*, "Enhanced Nonlinear Emission from Single Multilayered Metal–Dielectric Nanocavities Resonating in the Near-Infrared," ACS Photonics **8**(2), 512–520 (2021).
8. M. Z. Alam, S. A. Schulz, J. Upham, *et al.*, "Large optical nonlinearity of nanoantennas coupled to an epsilon-near-zero material," Nat. Photonics **12**(2), 79–83 (2018).
9. G. Li, S. Zhang, and T. Zentgraf, "Nonlinear photonic metasurfaces," Nat. Rev. Mater. **2**(5), 17010 (2017).
10. S. Palomba, M. Danckwerts, and L. Novotny, "Nonlinear plasmonics with gold nanoparticle antennas," J. Opt. A: Pure Appl. Opt. **11**(11), 114030 (2009).
11. S. H. Huang, H. P. Su, C. Y. Chen, *et al.*, "Microcavity-assisted multi-resonant metasurfaces enabling versatile wavefront engineering," Nat. Commun. **15**(1), 9658 (2024).
12. M. Nie, Y. Zhao, W. Nam, *et al.*, "Broadband Nanoscale Surface-Enhanced Raman Spectroscopy by Multiresonant Nanolaminate Plasmonic Nanocavities on Vertical Nanopillars," Adv. Funct. Mater. **32**(32), 2202231 (2022).
13. E. Mejia, Y. Qian, S. A. Safiabadi Tali, *et al.*, "Spectral tuning of double resonant nanolaminate plasmonic nanoantennas with a fixed size," Appl. Phys. Lett. **118**(24), 241108 (2021).
14. M. S. Bin-Alam, O. Reshef, Y. Mamchur, *et al.*, "Ultra-high-Q resonances in plasmonic metasurfaces," Nat. Commun. **12**(1), 974 (2021).
15. A. Larin, E. Kurganov, Y. Sun, *et al.*, "The Hybrid Metasurface Lights a Fire in Silicon: The Role of Plasmonic Nanogap Cavities in Multiphoton-Induced Broadband Photoluminescence," ACS Photonics **12**(8), 4323–4330 (2025).
16. N. L. Kazanskiy, S. N. Khonina, M. A. Butt, *et al.*, "A Numerical Investigation of a Plasmonic Sensor Based on a Metal-Insulator-Metal Waveguide for Simultaneous Detection of Biological Analytes and Ambient Temperature," Nanomaterials **11**(10), 2551 (2021).
17. M. G. Nielsen, A. Pors, O. Albrektsen, *et al.*, "Efficient absorption of visible radiation by gap plasmon resonators," Opt. Express **20**(12), 13311–13319 (2012).
18. M. G. Nielsen, D. K. Gramotnev, A. Pors, *et al.*, "Continuous layer gap plasmon resonators," Opt. Express **19**(20), 19310–19322 (2011).
19. N. Liu, M. Mesch, T. Weiss, *et al.*, "Infrared perfect absorber and its application as plasmonic sensor," Nano Lett. **10**(7), 2342–2348 (2010).
20. F. Yang, "Resonance and sensing characteristics of horn-shaped cavity-coupled MIM waveguide," AIP Adv. **12**(6), 065019 (2022).
21. H. Su, S. Yan, X. Yang, *et al.*, "Sensing Features of the Fano Resonance in an MIM Waveguide Coupled with an Elliptical Ring Resonant Cavity," Appl. Sci. **10**(15), 5096 (2020).
22. K. Ueno, J. Yang, Q. Sun, *et al.*, "Control of plasmon dephasing time using stacked nanogap gold structures for strong near-field enhancement," Appl. Mater. Today **14**, 159–165 (2019).
23. W. Nam, W. Kim, W. Zhou, *et al.*, "A digital SERS sensing platform using 3D nanolaminate plasmonic crystals coupled with Au nanoparticles for accurate quantitative detection of dopamine," Nanoscale **13**(41), 17340–17349 (2021).
24. J. Song, W. Nam, and W. Zhou, "Scalable High-Performance Nanolaminated SERS Substrates Based on Multistack Vertically Oriented Plasmonic Nanogaps," Adv. Mater. Technol. (Weinheim, Ger.) **4**, 1800689 (2019).
25. J. Song and W. Zhou, "Multiresonant Composite Optical Nanoantennas by Out-of-plane Plasmonic Engineering," Nano Lett. **18**(7), 4409–4416 (2018).
26. T. Moon, H. Joo, B. Das, *et al.*, "Adaptive Gap-Tunable Surface-Enhanced Raman Spectroscopy," Nano Lett. **24**(12), 3777–3784 (2024).
27. X. Gu, J. Li, Z. Liang, *et al.*, "Multilayer all-dielectric metasurfaces expanding color gamut," Nanophotonics **13**(19), 3749–3763 (2024).
28. N. E. Esfahani, J. Kovác, G. Maruccio, *et al.*, "Comparative Analysis of Two Different MIM Configurations of a Plasmonic Nanoantenna," Plasmonics **20**(6), 3265–3279 (2024).
29. L.-H. Yao, Z.-W. Ma, X.-Y. Song, *et al.*, "Broadband light generation from Au–Al2O3–Al sub-10 nm plasmonic gap structures," J. Mater. Chem. C **5**(27), 6771–6776 (2017).
30. X. Chen, H. R. Park, M. Pelton, *et al.*, "Atomic layer lithography of wafer-scale nanogap arrays for extreme confinement of electromagnetic waves," Nat. Commun. **4**(1), 2361 (2013).

Optics EXPRESS

31. R. Das, S. Sarkar, M. Saha, *et al.*, "Two peak luminescence from linoleic acid protected gold nanoparticles," J. Lumin. **168**, 325–329 (2015).
32. Y. Yan, F. Li, J. Shen, *et al.*, "Highly Intelligent Forward Design of Metamaterials Empowered by Circuit-Physics-Driven Deep Learning," Laser Photonics Rev. **19** (2024).
33. M. Dareini, S. R. Ghorbani, H. Arabi, *et al.*, "Application of circuit model for gap-plasmon nanodisk resonators," Photonics Nanostructures: Fundam. Appl **60**, 101264 (2024).
34. J. Xiong, J. Shen, Y. Gao, *et al.*, "Real-Time On-Demand Design of Circuit-Analog Plasmonic Stack Metamaterials by Divide-and-Conquer Deep Learning," Laser Photonics Rev. **17** (2022).
35. J. Zhu, L. Zhang, S. Jiang, *et al.*, "Selective light trapping of plasmonic stack metamaterials by circuit design," Nanoscale **12**(3), 2057–2062 (2020).
36. A. R. Rashed, M. Habib, N. Das, *et al.*, "Plasmon-modulated photoluminescence enhancement in hybrid plasmonic nano-antennas," New J. Phys. **22**(9), 093033 (2020).
37. T. Ngoc Lle, J. Wiedemair, A. van den Berg, *et al.*, "Plasmon-modulated photoluminescence from gold nanostructures and its dependence on plasmon resonance, excitation energy, and band structure," Opt. Express **23**(5), 5547–5564 (2015).
38. C. Lumdee, B. Yun, and P. G. Kik, "Gap-Plasmon Enhanced Gold Nanoparticle Photoluminescence," ACS Photonics **1**(11), 1224–1230 (2014).
39. H. Hu, H. Duan, J. K. Yang, *et al.*, "Plasmon-modulated photoluminescence of individual gold nanostructures," Acs Nano **6**(11), 10147–10155 (2012).
40. C. Chen, S. Kim, S. Behera, *et al.*, "Plasmonic nanogap grid arrays for tunable SERS enhancement and strain-induced shifts in 2D materials," Opt. Express **33**(20), 41833–41844 (2025).
41. I. Kochylas, A. Dimitriou, M. A. Apostolaki, *et al.*, "Enhanced Photoluminescence of R6G Dyes from Metal Decorated Silicon Nanowires Fabricated through Metal Assisted Chemical Etching," Materials **16**(4), 1386 (2023).
42. O. A. Yeshchenko, I. S. Bondarchuk, V. V. Kozachenko, *et al.*, "Photoluminescence of rhodamine 6G in plasmonic field of Au nanoparticles: Temperature effects," J. Lumin. **158**, 294–300 (2015).
43. M. Kaur, G. A. Mandl, S. L. Maurizio, *et al.*, "On the photostability and luminescence of dye-sensitized upconverting nanoparticles using modified IR820 dyes," Nanoscale Adv. **4**(2), 608–618 (2022).
44. C. Nien, L.-C. Chang, J.-H. Ye, *et al.*, "Proximity effect correction in electron-beam lithography based on computation of critical-development time with swarm intelligence," J. Vac. Sci. Technol. B **35**(5), 051603 (2017).
45. Y. Chen, "Nanofabrication by electron beam lithography and its applications: A review," Microelectron. Eng. **135**, 57–72 (2015).